Possibilities for UXO Classification Using Characteristic Modes
Of the
Broad-band Electromagnetic Induction Response

D.D. Snyder, Scott MacInnes, Scott Urquhart, and K.L. Zonge
Zonge Engineering and Research Organization, Inc.
3322 E. Fort Lowell Rd., Tucson, Arizona USA 85716

1.0 INTRODUCTION

The measurement of the broadband induction electromagnetic response in the form of a complex function of frequency (FEM) or, alternatively, as a transient function of time (TEM) has been applied in geophysical exploration for 30 years or more. Broadband EM methods are used in exploration in two different ways [1] [2]: 1) to perform "soundings" wherein the objective is to map the earth conductivity as a function of depth, and 2) for "inductive prospecting" wherein the broadband response permits the detection and characterization of large highly conductive "ore bodies" at great depth. Until recently, broadband induction EM methods were not routinely applied for shallow exploration problems. The principles of the induction EM method require that as the geometric scale of the problem decreases, there must be a corresponding broadening of the frequency range of interest in FEM systems or, equivalently, shortening of the time interval of interest in TEM systems [3]. At present only a few field instruments are available with the requisite bandwidth for effective application to sounding or prospecting in the shallow subsurface (< 30 m).

Elementary induction EM principles are also applied in metal detectors and as such they have enjoyed a long and successful history in applications such as utilities location and in the location of metallic mines. Metal detectors are typically optimized for detecting very small objects located within a few 10's of cm from the surface. Recently, however, new induction EM instruments have been developed specifically for shallow metal detection and site characterization [4] [5]. These instruments have significantly increased the depth of detection for shallow-buried metallic objects and, at least in one case, they provide measurements at more than one frequency or time delay. These instruments are now widely applied for detecting and mapping shallow-buried metal objects including UXO.

The potential for using the characteristics of the broadband induction EM response measured in the proximity of buried metallic objects to discriminate target types is generally recognized. In the context of UXO detection with TEM, McNeill et. al. [5], concluded that *". . ., given "a priori" knowledge of the decay characteristics of UXO that are expected in a survey area, the evidence presented in this paper suggests that it might be possible to separate out various types of UXO (a) from each other and (b) from exploded ordnance and other trash metal."* Moreover, there is ongoing research and development directed toward developing instruments and techniques for object detection and classification with broadband induction EM [6].

In cooperation with Earth Tech, Zonge Engineering has been investigating how a fast TEM system might be applied for UXO characterization. In this paper, we explore how broadband induction EM responses (i.e., TEM transients, or FEM spectra) can provide a basis for UXO classification. In that regard, the next section will review briefly some important characteristics of the inductive EM response of confined conducting and permeable objects. These characteristics, long recognized by exploration geophysicists,

provide a basis for expanding an FEM spectrum or TEM transient as a series of *characteristic modal functions* whose parameters contain information about the conductivity and size characteristics of the target. One method for the decomposition of the EM response into these characteristic modes, Prony's method, is discussed briefly and is applied to both synthetic and real TEM transients. Finally, we present data acquired with a prototype antenna system consisting of a horizontal transmitting antenna and a 3-axis receiving antenna. With this antenna system, data were acquired using a Zonge 3-channel NanoTEM™ system.

2.0 THE BROADBAND EM RESPONSE OF CONFINED CONDUCTORS

Baum [7] has published a very complete theory for the low-frequency EM response of small highly conducting and magnetically permeable objects such as UXO. The theory of UXO detection and characterization with induction EM is simplified by making assumptions that, for the most part, are fully justified by the nature of the target. The assumptions are:

1) Most UXO, being fabricated from metallic shells, have high electrical conductivity relative to the soils in which they are buried. UXO conductivity is typically 6 or more orders of magnitude higher than the host medium. Thus, to a first approximation at least, we can assume that the host medium is non-conducting (i.e., $\sigma=0$). This greatly simplifies the analysis of the EM response in the presence of a piece of UXO.

2) UXO is fabricated from steel and has a magnetic permeability that runs as high as 200. Typical host soils have a relative permeability approaching 1. In most cases, therefore, the assumption of a host medium with magnetic permeability μ_0 is valid.

3) At the frequencies employed, UXO is electrically small. That is, the characteristic dimension of the UXO is very much smaller than a free-space wavelength of electromagnetic radiation in the host medium. This assumption permits us to use the so-called *quasi-static* approximation with regard to analysis of electromagnetic fields wherein EM propagation effects are ignored.

4) UXO has a fully three-dimensional geometry with characteristic dimensions that are small compared with the distance from the sensor array. To a good approximation, therefore, we can assume that the magnetic fields generated by the transmitter antennas are approximately uniform over the volume occupied by the UXO. Moreover, the secondary magnetic fields at the measurement point can be approximated by simple point dipole sources with a time or frequency-dependent moment.

The electromagnetic responses of bodies that satisfy assumptions 1-3 have been termed *confined conductors* by Kaufman [8]. Kaufman concludes that the spectrum of the magnetic field created by eddy currents in a confined conductor can be represented as the sum of simple poles located along the negative real axis. Baum and colleagues [7] [6] have developed a more general theory than Kaufman has for the EM response of confined conductors and they arrive at the same result. It is generally accepted that the induction EM response of confined conductors in the frequency domain is governed by a set of simple poles:

$$H(s) = \sum_{i=1}^{\infty} \frac{B_m}{s - s_m} \qquad (1)$$

where $H()$ = magnetic field intensity

         s = Laplace transform variable

         s_m = the mth pole of the induced magnetic field (all negative real numbers)

         B_m = the coefficient for the series expansion (mathematically termed the *residue* of the pole)

The corresponding time-domain expression for the magnetic field given in equation (1) is

$$h(t) = \sum_{m=1}^{\infty} B_m e^{s_m t} \qquad (2)$$

Values for the poles and residues (i.e., s_m, and B_m) can be determined analytically for only a few geometries whose surfaces correspond to coordinate surfaces of special orthogonal coordinate systems (e.g., spheres). Kaufman [9] has tabulated formulas for the principal (i.e., longest) time constants of various canonical shapes. Saito [10] has developed an empirical formula for the principal time constant for a thin rectangular plate. Saito also has determined an empirical relation for the equivalent magnetic moment of a rectangular plate. However, there are numerical methods for finding the poles and residues associated with the response of for arbitrary-shaped conductors [6].

2.1 Conducting Permeable Sphere

The sphere with finite conductivity and a magnetic permeability different from that of free space is a simple three-dimensional shape for which an analytic solution for the inductive EM response is available. We shall use the behavior of the sphere to illustrate the general behavior of the broadband EM response for the more general class of confined conductors. Wait [11] demonstrated that the magnetic field generated by a conducting non-permeable sphere in a non-conducting whole space behaves like a point dipole located at the center of the sphere when in the presence of a uniform time varying magnetic field. In a later paper, Wait and Spies [12] extended the theory to include the effect of magnetic permeability. The EM transient behavior of the sphere also appears in Baum [7] and in Sower [13]. The moment (*M*) of the dipole is parallel to the direction of the incident field and varies with time or frequency according to relations given

below. Spatial variations in the secondary magnetic field generated by eddy currents and/or static magnetic polarization in the sphere follow the mathematical behavior of the dipole [7].

$$\vec{H}_s = \frac{1}{4\pi\,r^5}\left[3(\vec{r}\vec{r}) - r^2 \vec{\vec{I}}\right]\cdot\left(\vec{\vec{M}}\cdot\vec{H}_0\right)$$

(3)

where (See Figure 1)

$\vec{H}_0, \vec{H}_s \Rightarrow$ the primary (inducing) and secondary (observed) magnetic fields, respectively

$\vec{M} = \vec{\vec{M}}\cdot\vec{H}_0 \Rightarrow$ Induced Magnetic Moment of the object

$\vec{\vec{M}} \Rightarrow$ Magnetic Polarizability Dyadic (Tensor /Matrix)

$\vec{\vec{I}} \Rightarrow$ The identity dyadic (Tensor/Matrix)

$r = |\vec{r}| \Rightarrow$ The position vector directed from the dipole (source point) to P, the field point.
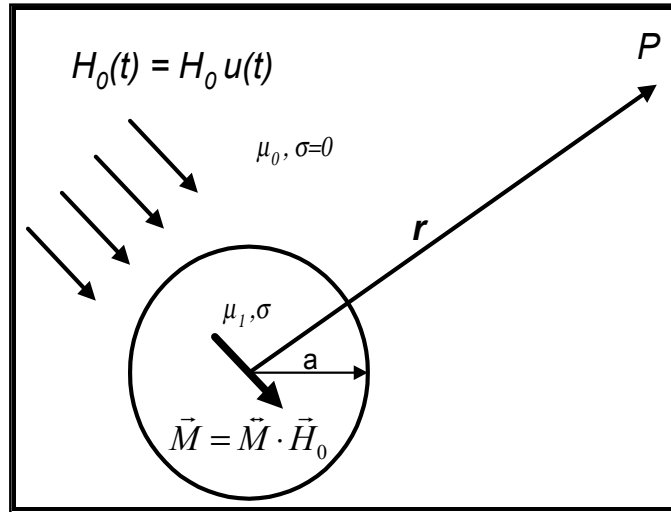

$H_0(t) = H_0\, u(t)$

$\mu_0,\ \sigma=0$

P

r

μ_1, σ

a

$\vec{M} = \vec{\vec{M}}\cdot\vec{H}_0$

Figure 1: Conducting and permeable sphere in a uniform field

The behavior of the secondary field (H_s) as a function of frequency or time is entirely contained in the moment term of equation (3). All other terms are purely geometrical. The direction of the moment is controlled by the direction of the primary field (H_0) and the magnetic polarizability dyadic ($\vec{\vec{M}}$). The location of the dipole target in space can be determined by the classical methods of magnetic exploration

and is treated at some length by Wynn [14]. Note that this does not necessarily mean that a magnetometer survey is required to independently establish target location. Its clear, for example, that the EM61 can do an adequate job of locating targets in the horizontal plane. A system similar to the EM61 having a tri-axial receiver can, in principle, provide the necessary additional information to estimate the three-dimensional target position. Once the dipole has been located, time or frequency variations in its moment may provide useful information about the classification of the target. In what follows, we restrict our analyses to that of the time-domain or transient behavior of the moment. We use the time domain in this paper. Keep in mind, however, that there exists a parallel approach for the analysis of equivalent broadband frequency-domain spectra.

The solution for the transient response for the conducting permeable sphere (see Figure 1) in a uniform non-conducting medium when illuminated by a constant uniform field that starts abruptly at time $t=0$ is [12] [15] [16]

$$h(t) = \left[6K \sum_{n=1}^{\infty} \frac{e^{-\frac{\delta_n^2 T}{K}}}{(K+2)(K-1)+\delta_n^2} - \frac{2(K-1)}{K+2} \right] u(T) \tag{4}$$

where

$h(t) = m(t)/2\pi a^3 H_0$ = normalized transient magnetic field moment

K = relative magnetic permeability $(\mu_1=K\mu_0)$

$T = t/(\mu_0 \sigma a^2)$ dimensionless time

δ_n = Solutions to $\quad \tan \delta_n = \dfrac{(K-1)\delta_n}{K-1+\delta_n^2}$ $\qquad\qquad$ (4a)

$u(t) = 0 \ (t < 0)$

$\qquad = 1 \ (t > 0)$

While there are TEM systems that can measure the step response (4) directly [17], most TEM systems, including the Zonge system used in this paper, measure the impulsive response, the time derivative of equation (4).

$$\frac{dh(t)}{dt} = \left[\delta(t) - 6K \sum_{n=1}^{\infty} \frac{\delta_n^2 \, e^{-\frac{\delta_n^2 T}{K}}}{(K+2)(K-1)+\delta_n^2} \right]$$ (5)

The transient behavior of magnetic fields generated by the magnetic dipole moment implied in (3) and (4) is therefore characterized by an infinite number of simple poles as suggested in (2) or, equivalently, time constants. Figure 2 shows plots of the transients generated by equation (5) for a number of values of the relative permeability parameter (K). Figure 2 uses the dimensionless time ($T = t/(\mu_0 \sigma a^2)$). Assuming that the target is composed of steel ($\sigma \approx 10^6$ S/m), one can obtain a time scale in microseconds by multiplying by the factor $126a^2$, where a is the radius of the sphere in centimeters. We included a linear plot of the decay curve to show that these curves are best displayed either in semi-log format (center) or log-log format (bottom). The exponential behavior of the TEM decay transient for confined conductors is best illustrated in the semi-log plot (center) where the curves exhibit a log-linear behavior at late times. The large dynamic range of TEM transients both in time and in amplitude makes it to display the transients as log-log plots (bottom). Although not appropriate to our discussions here, TEM decay transients observed over a semi-infinite medium where host conductivity is significant decay in time according to a power law. The physics of the TEM method for large-scale exploration problems suggests that TEM decay transients are best displayed on a log-log plot. The log-log plot indicates that the variation in TEM decay curves for objects can span more than 3 decades in time as a function of relative permeability. Note also that at high (e.g. K>50), the transient curve exhibits a near log-log linear behavior (Figure 2 – bottom). This behavior emphasizes the significance of the shorter time constants in TEM decay transients from targets with high K.

Figure 3 (after Sower [13]) plots the difference ($\delta_n - n\pi$) as a function of n, where δ_n are solutions to equation (4a) above. Note that for the case $K=1$, the solution of (4a) is precisely $\delta_n = n\pi$. This figure shows that the time constants in equations (4) and (5) vary significantly with K as well as with the radius a and the conductivity σ. Therefore, provided we can analyze the transient behavior and determine the values of the time constants $\tau = K \mu_0 \sigma a^2/\delta_n^2$ and the residues B_m (equation 2), this information would provide the basis for determining unknown parameters for the sphere including the electrical conductivity (σ), relative permeability (K), and sphere radius (a). The poles and residues are plotted as time-constant spectra in the plot on the right hand side of Figure 4. Here we have plotted the theoretical time constants ($\tau/\mu_0 \sigma a^2 = K/\delta_n^2$) on a logarithmic scale versus the log of the relative permeability (K = 1,2,5,20,50,100,200). The pixel points representing the time constant have been color modulated on a logarithmic scale in an effort to provide a sense of the amplitude of the residues involved. Only 20 of the time constants for each of the transient curves have been shown. The time-constant spectra exhibit a near log-log linear behavior of the time-constants as a function of relative permeability. The range of relative permeability ($1 \le K \le 200$) was

chosen to be representative of what might be encountered in UXO detection with K=200 being an estimate for the effective relative permeability of steel in the presence of a small polarizing field ($H_0 \approx O[1A/m]$).[1]

2.2 Analysis by Characteristic Modes

To take advantage of the physics governing the behavior of the broadband EM responses from confined conductors, it is necessary to decompose or parameterize the response into parameters defining the location and residue of the poles or, equivalently, values for the time constants and the corresponding series coefficients. The residues, of course, will be functions of the position of the receiver with respect to the target (r), and the amplitude of the primary magnetic field (H_0). The poles, however, are intrinsic characteristics of the target and are like the **natural** or **characteristic** frequencies of many dynamical systems.

Techniques for computing the time constants and the coefficients or, equivalently, the poles and residues have been frequently described in the literature over the last 25 or more years [18] [19] [20] [21]. The development or, more appropriately, the perfection of techniques for pole extraction in recent years has apparently been driven by the need to classify targets based on the analysis of the transient radar and sonar returns. We have chosen Prony's method, described in modern literature by Hildebrand [22], to use in analyzing both synthetic and real TEM transients. We make no representations as to the efficacy of this method for application to TEM transients. However, as suggested by the literature, the method has been useful for analysis of radar and sonar transients.

We will not describe Prony's method in great detail. But it is useful to describe the method in general. The mathematical model of the transient is based on equation (2). We suppose that there is available a sampled TEM decay transient consisting of a uniformly sampled time series $h(n\Delta t)$ of length $2N$ that we suppose can be parameterized by a set of N poles and residues $\{s_n, B_n\}$ satisfying equation (2)

$$h(n\Delta t) = h_n \cong \sum_{m=1}^{N} B_m e^{s_m n\Delta t} \tag{6}$$

The uniformly sampled transient (h_n) must satisfy a difference equation of order N that can be written as

$$\sum_{i=0}^{N} \alpha_i h_{i+j} = 0, \quad i + j = n = 0,1,...,2N-1 \tag{7}$$

---

[1] Sower [13] observes that the relative permeability of ferrous objects is a function of the field strength of the polarizing field. While at low field strengths the permeability is 200, that permeability can reach as high as 5000 at higher field strengths. He notes that most commercially available iron and steel saturates at a field strength of about 80 A/m, a value which is easily generated by a multi-turn transmitter loop carrying several amperes of current.

The roots of the algebraic equations

$$\sum_{i=0}^{N} \alpha_i Z^i = 0 \qquad (8)$$

are $Z_m = e^{s_m \Delta t}$, m = 1,2, . . .,N. If in (7) we set $\alpha_N = 1$, then the difference equation can be cast into the form of a set of N linear equations in the N unknown α_I:

$$\sum_{i=0}^{N-1} \alpha_i h_{i+j} = -h_{N+j} \qquad (9)$$

Once the α's have been found, they are used in equation (8) to find the N unknown roots Z_m. The residues B_m in equation (6) are then found by solving the N linear equations formed by substituting the roots $s_m \Delta t = log[Z_m]$ into (6) and forming at least N independent linear equations in the unknown residues B_m.

After verifying the program implementation of Prony's method using simple models consisting of a few time constants, we applied it to the data sets shown in Figure 2. The data sets were sampled using a dimensionless sample interval of 0.01. The results (Figure 5) are plotted in the form of transient curves plots showing the observed data (points), and the corresponding exponential curve fit (lines). The figure on the right, shows the time-constant spectra corresponding to each of the curves that were analyzed. The results show that the Prony analysis effectively resolves at least 3 of the poles. The obvious differences in the fit of the curves for K=5, and K=10 is caused by the choice of digitization interval.

3.0 EXPERIMENTAL DATA COLLECTION AND ANALYSIS

The foregoing analysis leads us to the conclusion that, in principle, the time-constant spectra provide a basis for the characterization or classification of small, buried, conducting/permeable targets such as UXO. As we have seen with the example of the sphere, these spectra are functions of relative permeability (K), conductivity (σ), and characteristic body dimension (a). However, before the time-constant spectra can be of significant benefit as a tool for target classification, it is first necessary to catalog these spectra for different shapes of interest either through analytical/numerical computations (as with the sphere model) or through experimental observations under controlled conditions. We know from the literature cited in this paper, for example, that it is possible to compute the characteristic modes or time constants for arbitrary shapes. The numerical problem is made simpler when the polarizing field is parallel to an axis of rotational symmetry. However, we have not yet developed programs that can perform the necessary numerical modeling for arbitrary target shapes and primary field excitations. Thus, previous knowledge of the behavior of time-constant spectra is confined to published relations for the values of the principal (i.e.,

longest) time constant appropriate for certain canonical shapes [9], and to experimentally-derived results reported by Saito [10], and Sower [16] [13]. These results report on the so-called late stage behavior of the TEM transient that is dominated by the principal time-constant.

3.1 Data Acquisition System

It is clear from modeling that the resolution of the higher order time constants of a TEM transient requires an fast TEM system with a large dynamic range (i.e., O[120db] after stacking). Zonge Engineering has developed a fast TEM system with acceptable specifications [23]. The NanoTEM™ consists of a small transmitter with a very fast turnoff time (~1 μs into low inductance loops) coupled together with a high-speed digital data acquisition system capable of simultaneously acquiring up to 3 channels of data at a maximum sample rate of 800 kSample/s on each channel. A measure of bandwidth of a TEM decay transient is the inverse of the current turnoff time ($1/T_0$). If the transmitter is turning off the current in 10μs, for example, the resulting decay transient will have a frequency bandwidth on the order of 100 kHz.[2] The NanoTEM system (the receiver plus transmitter) can generate and subsequently measure decay transients starting at delay times on the order of 1 μs out to delay times of several milliseconds. An equivalent broadband FEM system would have to sample the frequency spectrum over a range of $0.5 \leq f \leq 500$ kHz.

The elements of the system are shown Figure 6. The figure shows the transmitter with external battery (12Vdc) on the left. The receiver is on the right. In the background is a small (0.5m x 0.5m) transmitter coil. A 3-in steel ball (mill ball) is pictured inside the transmitter and receiving coils. The system, as shown in Figure 6, was used to measure decay transients from many of the smaller targets shown in Figure 7. We used the larger (5'x5') Helmholtz coil to acquire transients from large targets such as a 105mm projectile (see Figure 8). To simulate realistic survey conditions, we used the cart pictured in Figure 9. The cart consists of a 1m x 1m transmitter antenna together with 3 orthogonal ½ m x ½ m receiver antennas. The receiver shown in Figure 6 can simultaneously measure the 3 vector components of the transient field.

In normal deployment, the system acquires a stacked transient consisting of 31 samples on logarithmically changing intervals of time. An example of the transient data acquired with the small coil system (shown in Figure 6) is shown in Figure 10. The system is also able to record the full transient on a uniformly sampled interval either 1.6 μs (600 kS/s) or 1.2 μs (800 kS/s). These data correspond to the processed (i.e. gated) data plotted above, with the gates expanding in width with increasing time.

---

[2] The transmitter turnoff time into the loops used in this paper was less than 10 μs.

3.2 UXO Characterization Experiments

With the data acquisition system previously described, we first conducted experiments aimed at characterizing various pieces of UXO and other small objects (see Figure 7) in order to determine their characteristic TEM transient response under controlled stimulation. In these experiments, objects are placed in a known source field. The resulting transients are reduced as described below in order to obtain a measure of their magnetic polarizability.

3.2.1 Data Reduction for Magnetic Polarizability

Baum [7] provides us with a simple model, the point dipole, for the induction EM response of a small object in the presence of a uniform time-varying primary magnetic field (H_0). The magnetic moment of the object is given by the relation $\vec{M} = \ddot{M} \cdot \vec{H}_0$, where $\ddot{M}$ is called the magnetic polarizability dyadic. The use of a dyadic or tensor to describe the polarizability of a target provides for the likelihood that, unlike the conducting permeable sphere which has isotropic polarizability, most UXO's will be anisotropically polarizable. That is, in general, the magnetic moment that is induced at the target by the incident (primary) field will not lie in the same direction as the field. Baum [24] has written extensively about the properties of the polarizability dyadic. He points out that it is a symmtric matrix that is, in general, *aspect* dependent. Its properties are dependent on a coordinate system fixed to the target. In the context of equation (3), therefore, the polarizability dyadic is a function of three aspect angles (e.g., heading, pitch, and roll) that the UXO-fixed coordinate system makes with the measurement axes (generally, x and y are horizontal coordinates, while z is in the vertical direction). Baum notes that the polarizability dyadic can usually be put into a coordinate system in which the dyadic is a diagonal matrix. This coordinate system is called the *principal coordinate system*. Moreover, if there are symmetries in the target (as there are in most UXO), the polarizability dyadic will be invariant under rotation about the axis of symmetry. In the case of the sphere, therefore, is is clear that the polarizabilty dyadic is isotropic and proportional to the identity matrix. Thus

$$\ddot{M} = \frac{m(t)}{H_0}\ddot{I} = \frac{m(t)}{H_0}\begin{bmatrix} 1 & 0 & 0 \\ 0 & 1 & 0 \\ 0 & 0 & 1 \end{bmatrix} \tag{10}$$

In those cases where UXO exhibits a single axis of cylindrical symmetry (say, the z-axis in the *principal system*), the polarizability dyadic will take the form

$$\ddot{M} = \begin{bmatrix} P_T(t) & 0 & 0 \\ 0 & P_T(t) & 0 \\ 0 & 0 & P_L(t) \end{bmatrix} = \frac{1}{H_0}\begin{bmatrix} m_T(t) & 0 & 0 \\ 0 & m_T(t) & 0 \\ 0 & 0 & m_L(t) \end{bmatrix} \tag{11}$$

where the subscript T signifies polarization that occurs when the field is transverse to the axis of symmetry while the subscript L signifies polarization that occurs when the incident field is parallel to the axis of symmetry. UXO generally has an axis of cylindrical symmetry and therefore we can use equation (11) to determine polarizability dyadic simply by measuring the TEM transient when the primary field (H_0) is aligned parallel (L) to the axis of symmetry (measure $m_L(t)$) and then by measuring the transient when the primary field is aligned transverse (T) to the axis of symmetry (measure $m_T(t)$). Provided we know the strength of the primary field, the polarizability dyadic can be found using (11).

We have measured the transients generated by a variety of targets (see Figure 7) that were placed at the center of either a single loop transmitter (shown in Figure 6) or a larger Helmholtz transmitter array (shown Figure 8). The receiver in both setups is a multi-turn square loop centered on the target. To a good approximation, the inducing field of the two transmitter antennas at the center of the antennas is, respectively,

$$H_0 = 3.55\,I \ \ A/m \Rightarrow .5m\,x.5m\,loop\,(2\,turns), \tag{12}$$

and,

$$H_0 = 5.90\,I \ \ A/m \Rightarrow 5\,ft\,Helmholtz\,Coil\,(4\,turns) \tag{13}$$

Now a dipole with moment $m(t)$ that is centered in a circular[3] coil (with N_r turns) having radius a and directed perpendicular to the plane of the coil, will generate a voltage given by the relation

$$v(t) = -\frac{\mu_0 N_r}{2a}\frac{dm(t)}{dt} = \sum_{i=1}^{N} B_i e^{-\frac{t}{\tau_i}} \tag{14}$$

We then use a method such as Prony's method to find the residues and time constants indicated on the right side of equation (14).

By integrating equation (14) with respect to time (t), we find a relation for the effective moment of the dipole

$$m(t) = \frac{2a}{\mu_0 N_r}\int_{\infty}^{t} v(t)dt = \frac{2a}{\mu_0 N_r}\sum_{i=1}^{N}\tau_i B_i e^{-\frac{t}{\tau_i}} \tag{15}$$

Using equation (11) with (15) above, we obtain a relation for magnetic polarizability

$$P(t) = \frac{2a}{\mu_0 N_r H_0} \int_\infty^t v(t)dt = \frac{2a}{\mu_0 N_r H_0} \sum_{i=1}^N \tau_i B_i e^{-\frac{t}{\tau_i}}$$ (16)

3.2.2 Polarizability Characterization Experiments

Objects were placed in the (assumed uniform) field of either the small (0.5m x 0.5m) coil or, for larger targets in the field of the 5ft x 5ft Helmholtz coil. In cases where the objects had an axis of symmetry, transients were measured with the field oriented parallel with the axis of symmetry and then with the field oriented perpendicular with that axis. Figures 11-15 show a few NanoTEM transients we have observed in the course of our characterization experiments. The data have been normalized for instrument gain and transmitter current only. The signal levels have not been adjusted to reflect either the transmitter or the receiver geometry and turns. For each object, we have plotted the observed data, together with its fit using the parameters obtained from Prony's decomposition on the left (labeled *Prony Fit*). The plot on the right (labeled *Time Constant Spectrum*) shows the values of the time constants obtained from the Prony analysis. The vertical position of the pixel represents the value of the time constant on a logarithmic scale shown on the left-hand side. The pixel has been color modulated (again on a logarithmic scale) to provide a sense of the relative amplitude of the residue corresponding to the associated time constant. The color bar on the right shows the color scale in accordance with the logarithmic scale shown on the right hand side of the plot. The magnetic polarizability value *P(0)* for each of the targets shown has been calculated using equation 16. The value of *P(0)* in units of cm^3 together with the principal (longest) time constant of the decomposition in units of µSec has been tabulated in Table 1. For targets having a single axis of azimuthal symmetry, we have plotted results for a primary field that is parallel with the symmetry axis (labeled 'L') and results for a primary field that is transverse to the symmetry axis (labeled 'T').

---

[3] In the analysis leading to the determination of normalization factors for computing moments and magnetic polarizability we have used the approximation that the voltage induced in a square coil of radius *a* may be approximated by the voltage that would be induced in a circular coil with the same cross sectional area.

Table 1: Polarizability and Principal Time Constants for Selected Test Objects

Target	$P(0)$ cm^3	τ_{max} (μs)
Spherical Handgrenade	19.0	356
20mm Projectile (L)	13.1	781
20mm Projectile (T)	3.3	580
M12 Handgrenade (L)	30.8	221
M12 Handgrenade (T)	24.0	264
2.25" Rocket (L)	13.5	1097
2.25" Rocket (T)	17.5	1113
3 2.5" Steel Washers	13.6	754
6 2.5" Steel Washers	22.4	884

3.2.3 UXO Survey Simulation

Other experiments were run using the antenna system shown in Figure 9. This system consists of a 1m x 1m transmitter antenna together with a set of 3 ½ m x ½ m tri-axial receiver coils oriented along the longitudinal (x), transverse (y), and vertical (z) directions. The receiver system shown in Figure 6 is able to simultaneously acquire data transients in each of the 3 orthogonal directions. With this antenna array, we have simulated surveys over targets buried at different depths in soil. Surveys were conducted in a "stop and go" mode wherein measurements were acquired at intervals of ½ m. We show here the results from a single profile of the vertical field component taken over a target consisting of a 1-ft length of 3.5" diameter steel pipe buried at a depth of 15" to its center. In this example, the pipe was buried so that its axis is vertical. Unfortunately, we have not measured the polarizability characteristics of this target. Our experiments continue, however, and we look forward to reporting results from the processing of a 3-component survey covering an area as opposed to a single component along a profile.

Six transients for the vertical component of the secondary fields are plotted in Figure 16. Each transient plot is annotated with the position (x) along the measurement profile. The target is located at x=2.5m. These transients display a sharp drop in the first decade (.001 to 0.01 ms). The decay continues to drop very fast for the 4 antenna positions (x=1.0,1.5,0,3.5,4.0). At times greater than 0.1 ms, the transients are at the instrument noise level (O[1μV]). In contrast, the 3 transients measured while the transmitter is at least partly over the target (i.e., x=2.0,2.5,3.0), exhibit extended responses that are above background and are coherent out to the end of the transient measurement time (1.911 ms). Figure 17 is a composite plot showing a simulation of an EM61 profile (top), and the time-constant spectra generated by Prony analysis. As with the characterization plots shown previously (Figures 12-16), the pixel location represents the value of the time-constant. The pixel color has been modulated to provide a sense of the amplitude of the residue. The time-constant spectra show that the longest time-constant is observed when the transmitter is centered directly over the target and hence the polarizing field H_0 is vertical and therefore parallel (Longitudinal) to

the target's axis of symmetry. In contrast, the transients measured ½ m on either side of the target exhibit a moderately lower time constant. These transients were observed at a point where a side of the transmitter loop was located directly over the target. In this case, the polarizing field is mostly horizontal and therefore corresponds to the case of transverse polarization with the incident field perpendicular to the axis of symmetry. This behavior is similar to the behavior of the axially symmetric objects we have tabulated in Table 1. Note also, that in this case the amplitude of the residues of the second time-constant is larger than that of the principal time constant. This is consistent with the behavior of the time-constant spectra for the conducting permeable sphere (see Figure 4). A conducting and non-permeable sphere exhibits residues having the same amplitude for each of the time-constants. However, Figure 4 shows that, as the permeability increases, the residues corresponding to the secondary time-constants can be larger than the residue for the principal time constant. The behavior of the time-constant spectra in Figure 8 therefore suggests that the target has high relative magnetic permeability.

4.0 CONCLUSIONS

In this paper we have used a method (Prony) to analyze the TEM decay curve to obtain a set of exponential decay time-constants and their corresponding residues. This approach has been applied for several decades to the analysis of radar and sonar reflection transients as an aid to target identification. Moreover, basic theory published in the geophysics literature and, more recently, in journals and books written by authors who approach the problem of UXO detection and discrimination from the military and security view point shows that the technique is equally applicable to the analysis of broadband induction EM data. We have acquired fast transient TEM (NanoTEM) data using a commercially available and field data acquisition system. However, the volume of raw data that is acquired with a 3-component TEM system measuring the full TEM decay transient would overwhelm us without a method of parameterization that is physically meaningful. We have shown that the transient data we acquire can be analyzed and displayed in a way that is simple to understand and provides information that is useful for classifying the TEM response.

The work presented here demonstrates a new TEM system, similar in many respects to the EM-61. The system has been assembled from commercially available and field-tested components, requiring only a specially designed mobile antenna system. The system is capable of acquiring 3-component TEM decay transients. These data can be quickly analyzed and displayed in a simple and physically meaningful way (time-constant spectra) that does not overwhelm the observer. Classification of targets will require additional processing steps aimed at comparing time-constant spectra such as those shown in Figure 18 with a library of magnetic polarizability dyadics. The work presented in Section 3.0 of this paper illustrates how such a library can be constructed from experimental data. An effort at constructing a more comprehensive library using both experimental data such as we generated here and data generated using numerical models is warranted. Finally, the reader should note that the polarizability characteristics of a library are only of

use when the target's 3-dimensional location is known. Location is required so that we may estimate H_0 at the location of the target and so estimate the polarizability using equation (16). As suggested in Figure 18, the polarizing magnetic field changes direction as the transmitter antenna moves with respect to the target. Therefore, in principal at least, the aspect angles of the target can be determined by measuring polarizability at different measuring points. But that is the subject of another paper. The location of the target in plan view is easily derived from a map generated from the TEM response for a single time gate similar to the EM61 metal detector. A qualitative estimate of target depth can also be generated. Naturally, the position of the target can also be estimated from independent data sets such as magnetometer survey. The availability of measurements of the 3-component transient field provides additional independent information at each measuring point. We are currently developing an algorithm for UXO target parameter estimation that will take advantage of the additional data acquired using the vector transient field. It is our belief that with these data, we can provide estimates of target parameters: position (3); aspect angles (2-heading and pitch); and polarizability (2 – longitudinal and transverse as functions of time).

5.0 REFERENCES

1. Nabighian, M.N., and James C. Macnae, *Time Domain Electromagnetic Prospecting Methods*, in *Electromagnetic Methods in Applied Geophysics, Volume 2, Application, Part A*, M.N. Nabighian, Editor. 1991, Society of Exploration Geophysicists: Tulsa, OK. p. 520.

2. Spies, B.R., and Frank C. Frischknecht, *Electromagnetic Sounding*, in *Electromagnetic Methods in Applied Geophysics, Volume 2, Application, Part !*, M.N. Nabighian, Editor. 1991, Society of Exploration Geophysicists: Tulsa, OK. p. 520.

3. Frischknecht, F.C., *Electromagnetic Physical Scale Modeling*, in *Electromagnetic Methods in Applied Geophysics Volume 1, Theory*, M.N. Nabighian, Editor. 1987, Society of Exploration Geophysicists: Tulsa, OK. p. 513.

4. Won, I.J., D.A. Keiswetter, G.R.A. Fields, G.R.A., and L.C. Sutton, *A new multifrequency electromagnetic sensor.* J. Environmental and Engineering Geophysics, 1996. **1**(2): p. 129-138.

5. McNeill, J.D., and Miro Bosnar. *Application of Time Domain Electromagnetic Techniques to UXO Detection.* in *UXO Forum 1996.* 1996. Williamsburg, VA.

6. Geng, N., Baum, Carl E., and Carin, Lawrence, *On the Low-Frequency Natural Response of Conducting and Permeable Targets.* IEEE Trans. on Geosci. and Rem. Sensing, 1999. **37**(1): p. 347-359.

7. Baum, C.E., *Low-Frequency Near-Field Magnetic Scattering from Highly But Not Perfectly Conducting Bodies*, in *Detection and Identification of Visually Obscured Targets*, C.E. Baum, Editor. 1999, Taylor & Francis: Philadelphia, PA.

8. Kaufman, A., *Frequency and Transient Responses of Electromagnetic Fields Created by Current in Confined Conductors.* Geophysics, 1978. **43**(5): p. 1002-1010.

9. Kaufman, A.A., *A Paradox in Geoelectromagnetism, and its Resolution, Demonstrating the Equivalence of Frequency and Transient Domain Methods.* Geoexploration, 1989. **25**: p. 287-317.

10. Saito, A., *Development of Transient Electromagnetic Physical Modeling for Geophysical Exploration*, in *Geophysics*. 1984, Colorado School of Mines: Golden, CO. p. 161.

11. Wait, J.R., *A Conducting Sphere in a Time Varying Magnetic Field.* Geophysics, 1951: p. 666-672.

12. Wait, J.R., and Kenneth P. Spies, *Quasi-static Transient Response of a Conducting Permeable Sphere.* Geophysics, 1969. **34**(5): p. 789-792.

13. Sower, G.D., *Eddy Current Responses of Canonical Metallic Targets*, in *Detection and Identification of Visually Obscured Targets*, C.E. Baum, Editor. 1999, Taylor & Francis: Philadelphia, PA. p. 243-282.

14. Wynn, W.M., *Detection, Localization, and characterization of Static Magnetic-Dipole Sources*, in *Detection and Identification of Visually Obscured Targets*, C.E. Baum, Editor. 1999, Taylor & Francis: Philadelphia, PA. p. 337-374.

15. Ward, S.H., and Gerald W. Hohmann, *Electromagnetic Theory for Geophysical Applications*, in *Electromagnetic Methods in Applied Geophysics-Theory*, M.N. Nabighian, Editor. 1987, Society of Exploration Geophysicists: Tulsa. p. 131-311.

16. Sower, G.D., *Eddy Current Responses of Canonical Metallic Targets - theory and Measurements*, . 1997, EG&G MSI. p. 34.

17. West, G.F., J.C. Macnae, and Y. Lamontagne, *A Time-Domain Electromagnetic System Measuring the Step-Response of the Ground.* Geophysics, 1981. **49**(7): p. 1010-1026.

18. Van Blaricum, M.L., and Mittra, Raj, *A Technique for Extracting the Poles and Residues of a System Directly from Its Transient Response.* IEEE Trans. on Ant. & Prop., 1975. **AP-23**(6): p. 777-781.

19. Van Blaricum, M.L., and Raj Mittra, *Problems and solutions Associated with Prony's Method for Processing Transient Data.* IEEE Trans Ant. and Propag., 1978. **AP-26**(1): p. 174-178.

20. Poggio, A.J., Michael L. Van Blaricum, Edmund K. Miller, and Raj Mittra, *Evaluation of a Processing Technique for Transient Data.* IEEE Trans. Ant. & Propag., 1978. **AP-26**(1): p. 165-173.

21. Moffatt, D.L., and K.A. Shubert, *Natural Resonances via Rational Approximants.* IEEE Trans. Ant. & Propag., 1977. **AP-25**(6): p. 657-660.

22. Hildebrand, F.B., *Introduction to Numerical Analysis*, . 1956, McGraw-Hill: New York. p. 378-382.

23. Mauldin-Mayerle, C., Norman R. Carson, and Kenneth L. Zonge. *Environmental Application of High Resolution TEM Methods*. in *The 4th Meeting on Environmental and Engineering Geophysics*. 1998. Barcelona, Spain: European Section, EEGS.

24. Baum, C.E., *The Magnetic Polarizability Dyadic and Point Symmetry*, in *Detection and Identification of Visually Obscured Targets*, C.D. Baum, Editor. 1999, Taylor & Francis: Philadelphia, PA. p. 219-242.
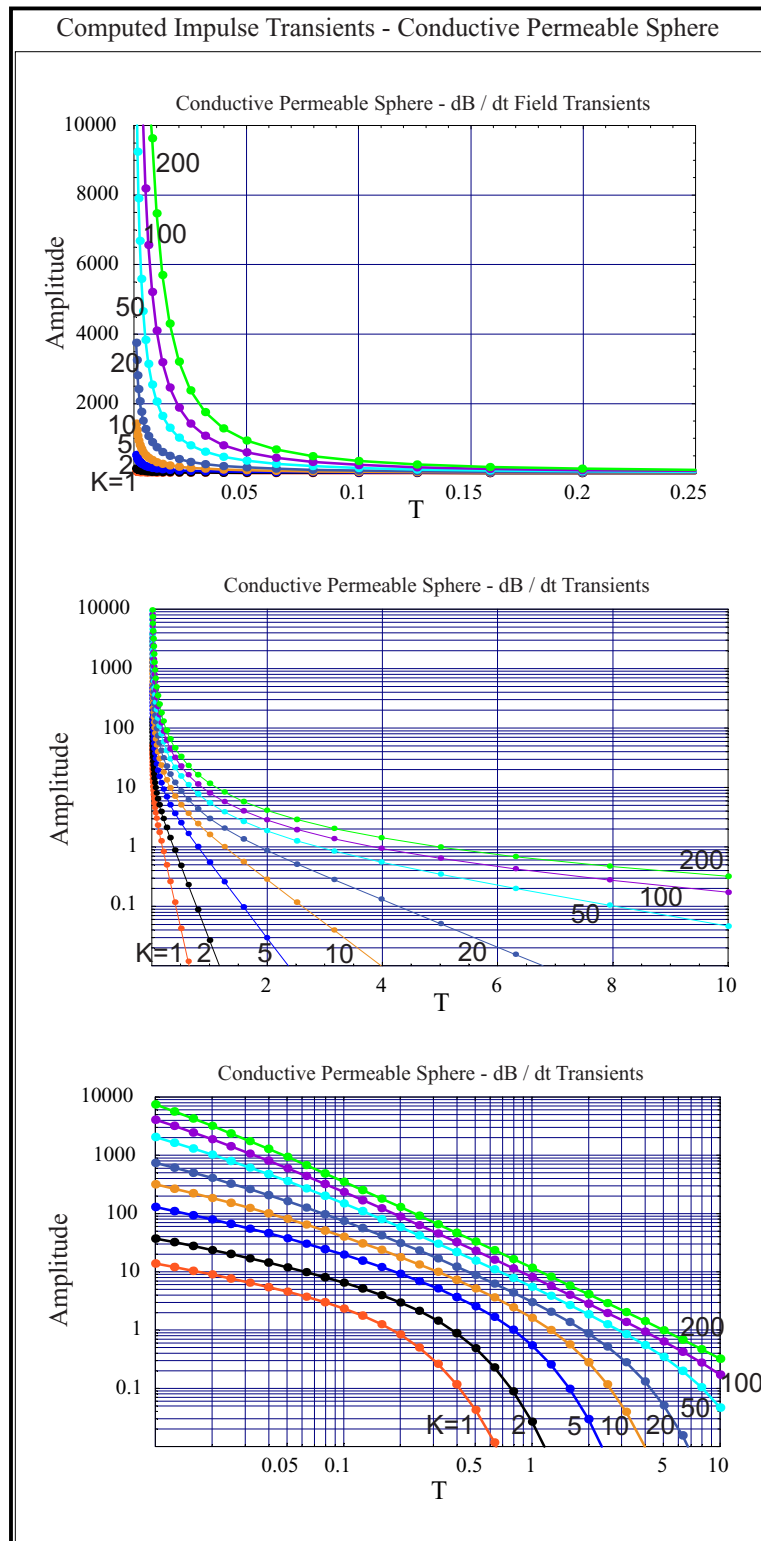
Figure 2: Computed Impulse Transients - Conductive Permeable Sphere
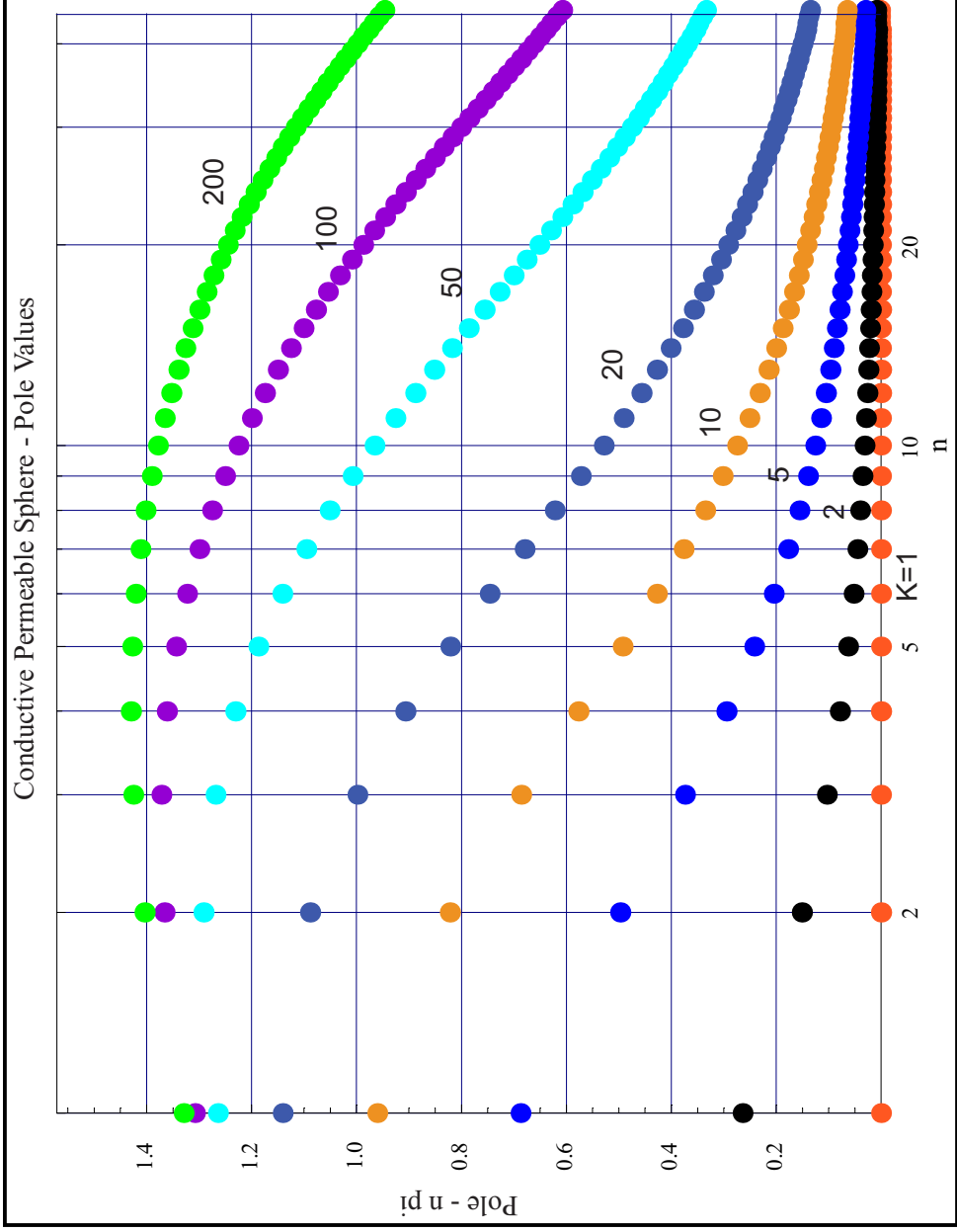
Figure 3: Deviation of characteristic pole position of a conducting permeable sphere as a function of series term (n) and parametrically as a function of relative permeability (K).

Computed Transients and Theoretical Time Constant Spectra
Conducting Permeable Sphere

Conductive Permeable Sphere - dB / dt Transients

Time Constant Spectra
Conducting Permeable Sphere
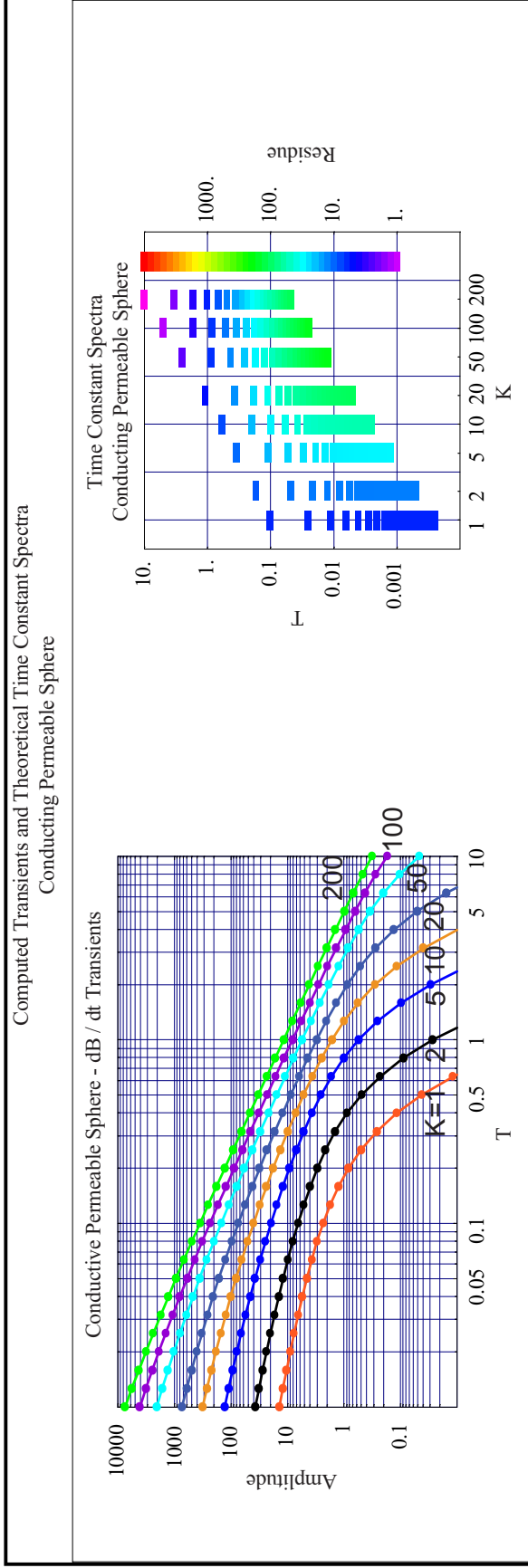
Figure 4: Time-constant spectra of theoretical TEM transients for a conducting permeable sphere.
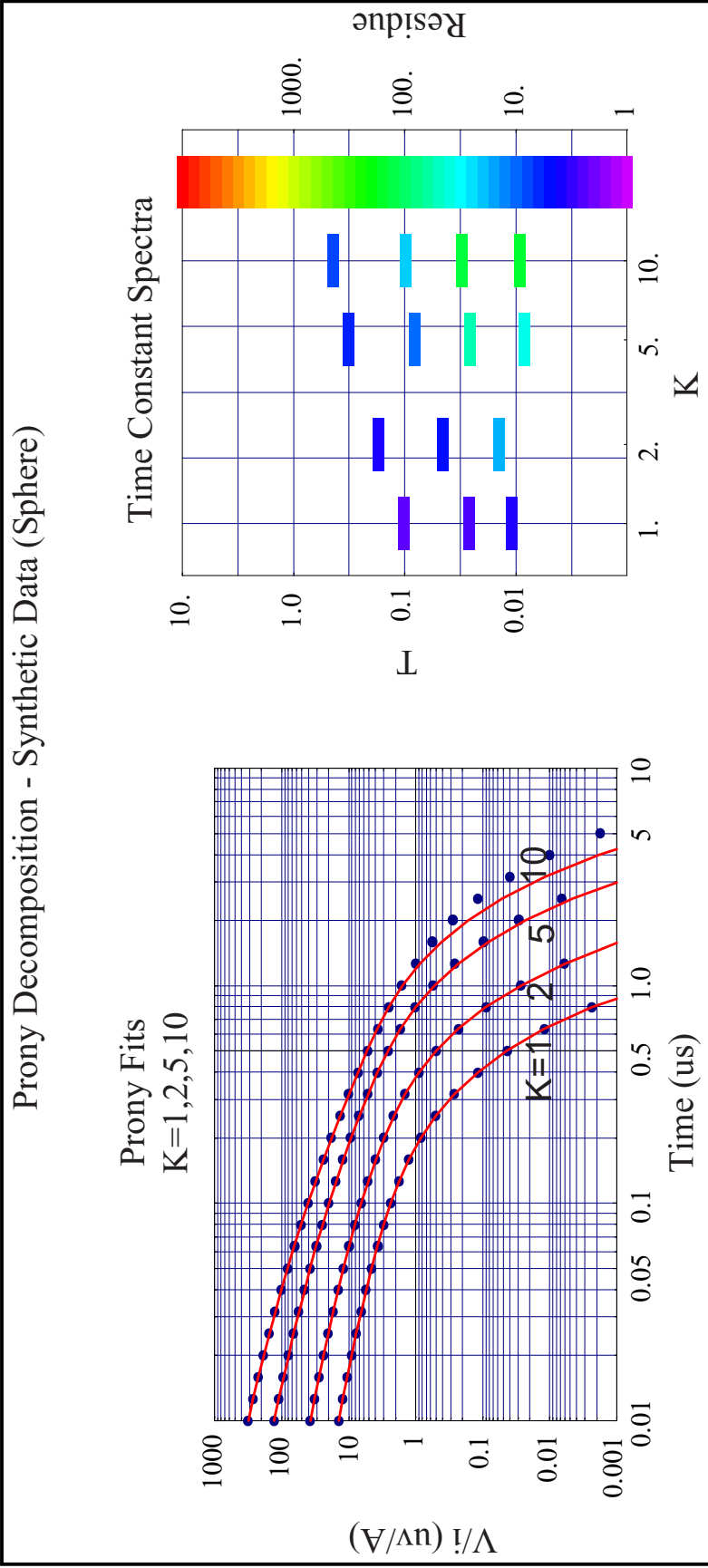
Figure 5: Time-constant spectra computed from numerical decay transients from a conducting permeable sphere.

Figure 6: Photograph showing the major components of the fast TEM system used to acquire experimental data. The system is shown connected to a small (.5m x .5m) transmitter coil used for characterization measurements on small targets.

Figure 7: UXO and other targets used in characterization experiments.
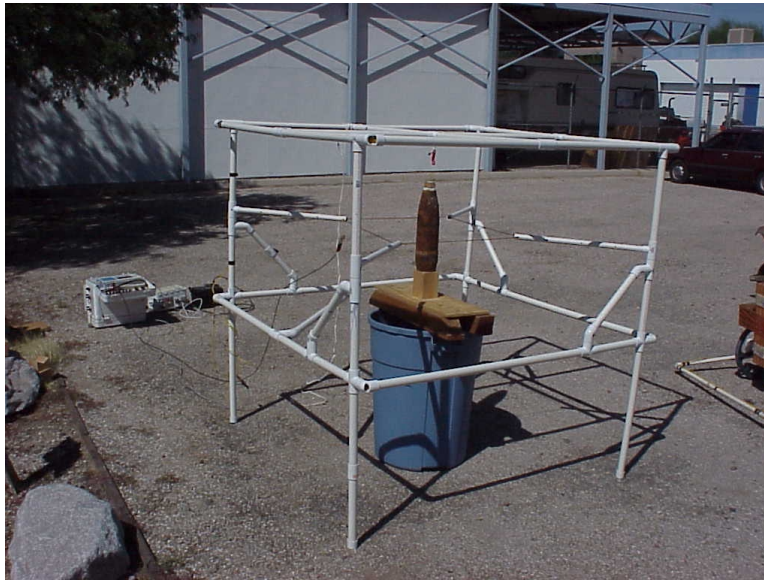
Figure 8: 5' x 5' Helmholtz transmitter antenna used for characterization measurements on large targets.
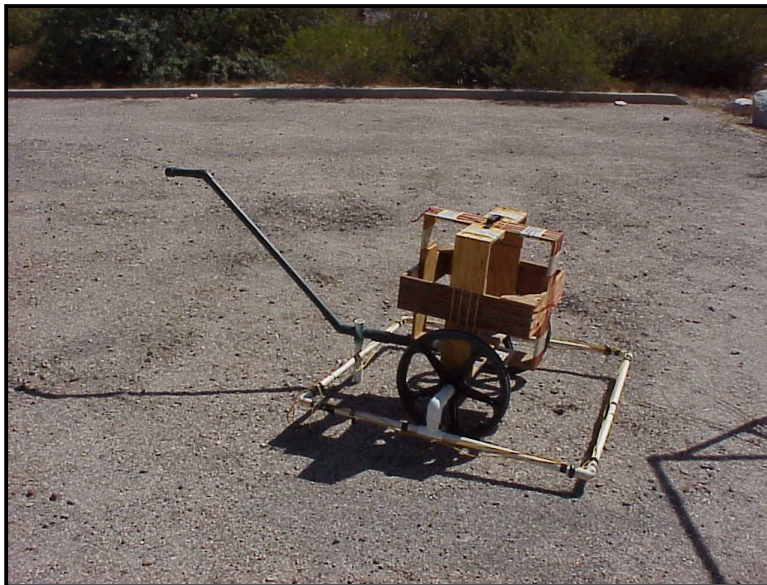
Figure 9: Experimental fast TEM antenna system for conducting simulated field experiments. The system consists of a 1m x 1m transmitter antenna and a 3 orthogonal 1/2m x 1/2m receiver antennas.
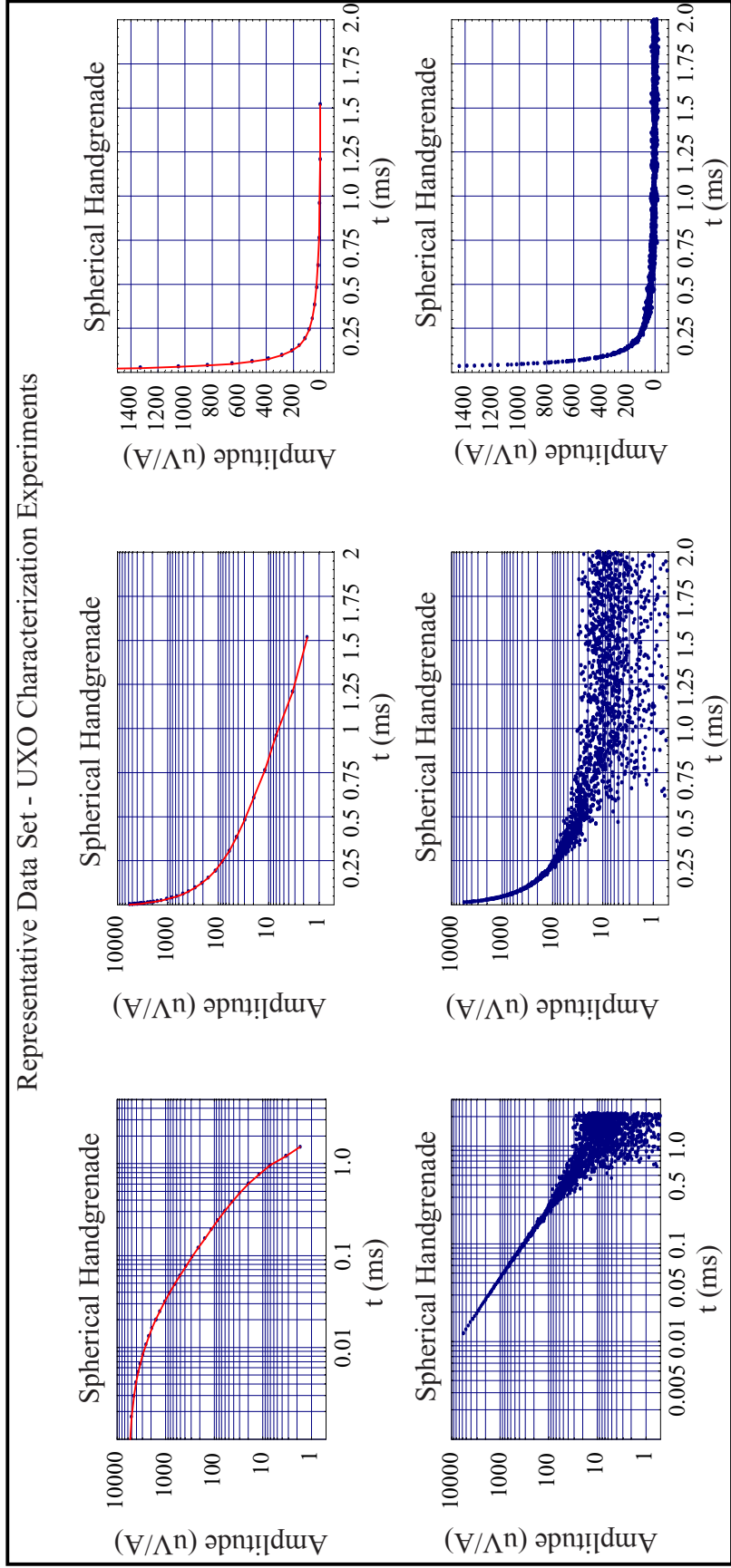
Figure 10: Typical NanoTEM transient data. Transients on top have been plotted from values of 31 logarithmically spaced windows. The plots below are uniformly sampled (1.2 us) data.
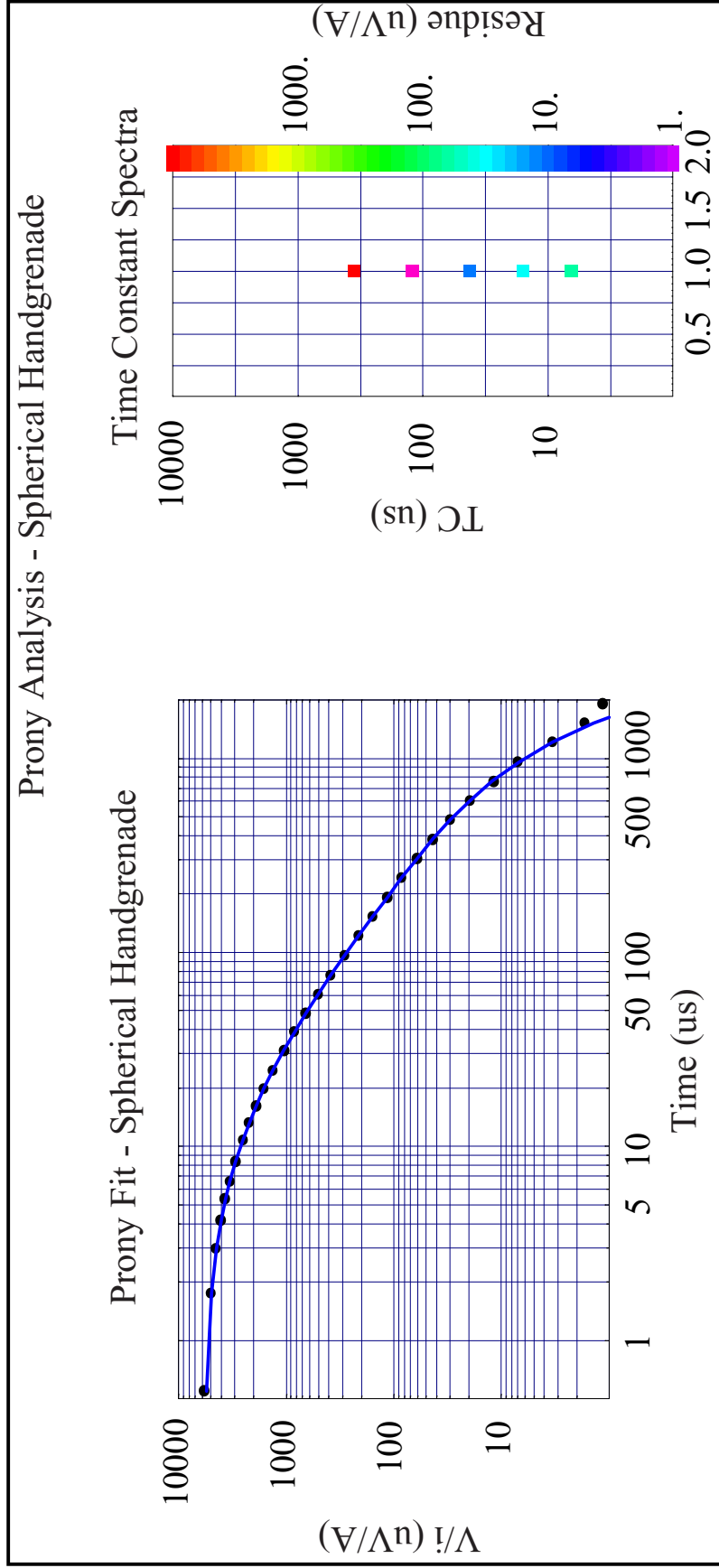
Figure 11: Prony analysis plot of TEM transients for a spherical handgrenade. The left hand side shows observed data (points) and parametric fit (line). The right hand side shows time constants for real poles found in the Prony analysis. The pixel has been color modulated according to the pole residue.
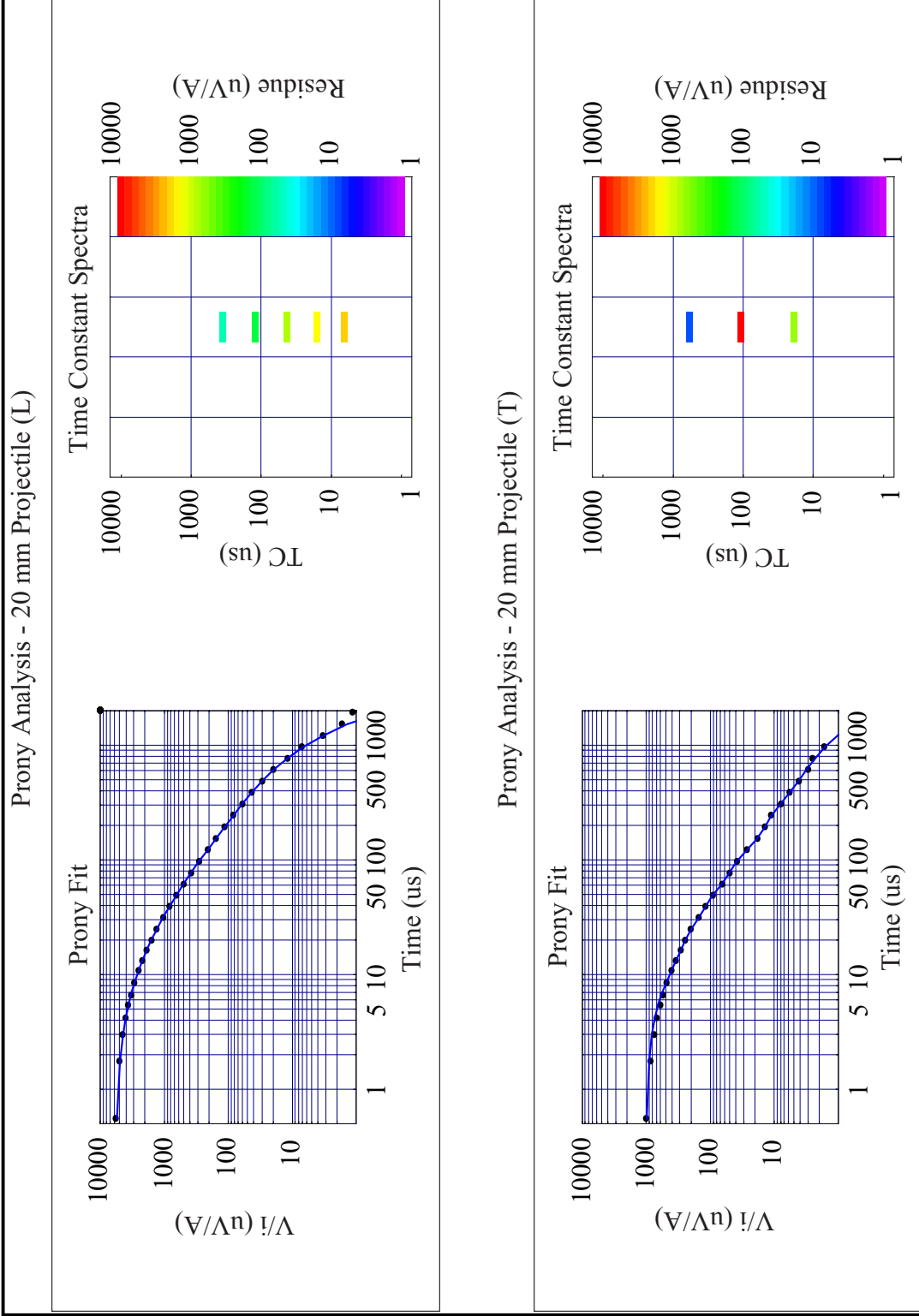
Figure 12: Prony analysis for TEM decay transients from a 20mm projectile. The upper plot is for a primary field that is parallel to the axis of symmetry. The lower plot is for the case of transverse polarization.
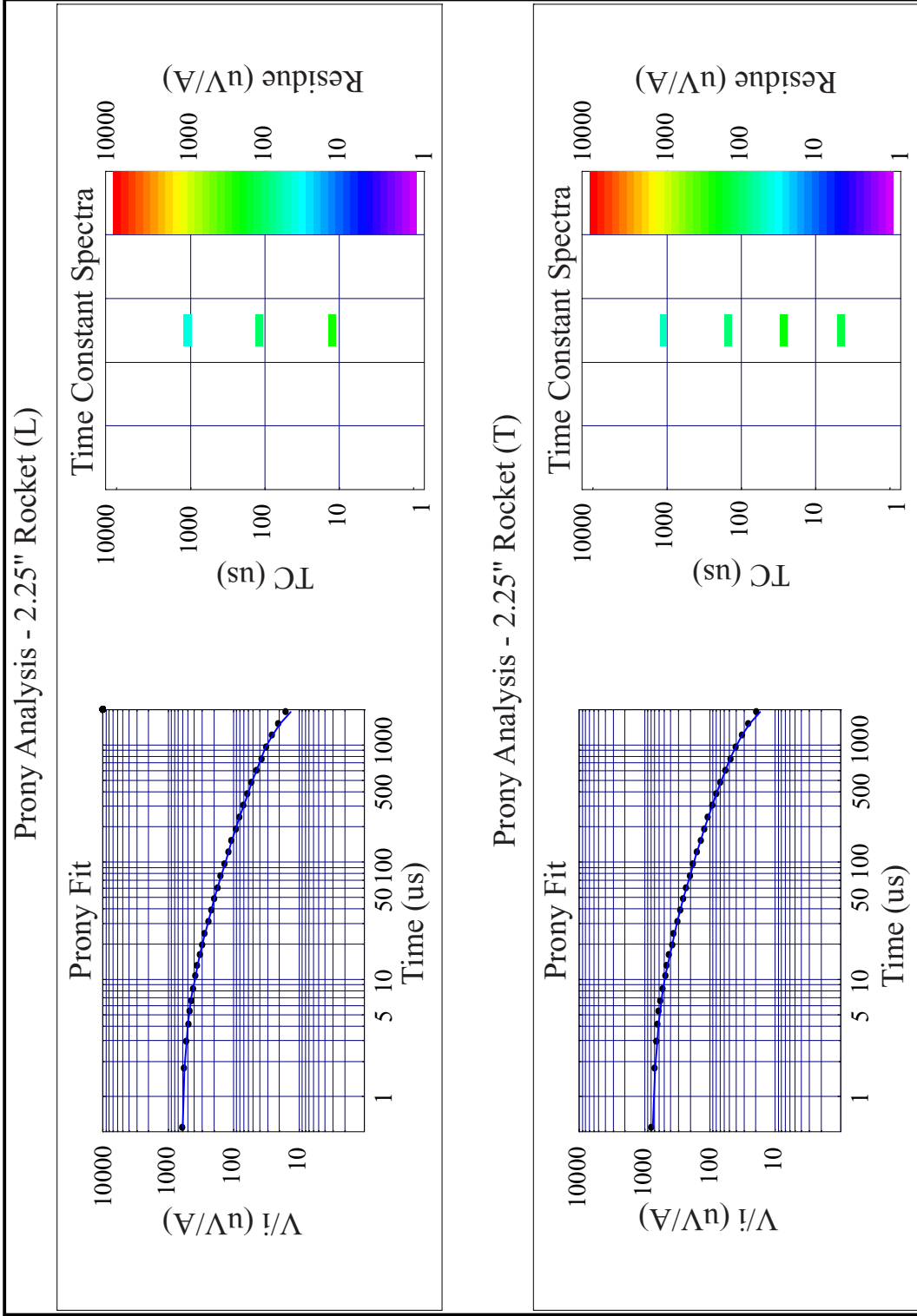
Figure 13: **Prony analysis for TEM decay transients from a 2.25" rocket head. The plot above is for longitudinal polarization (L). The plot below is for transverse polarization (T).**
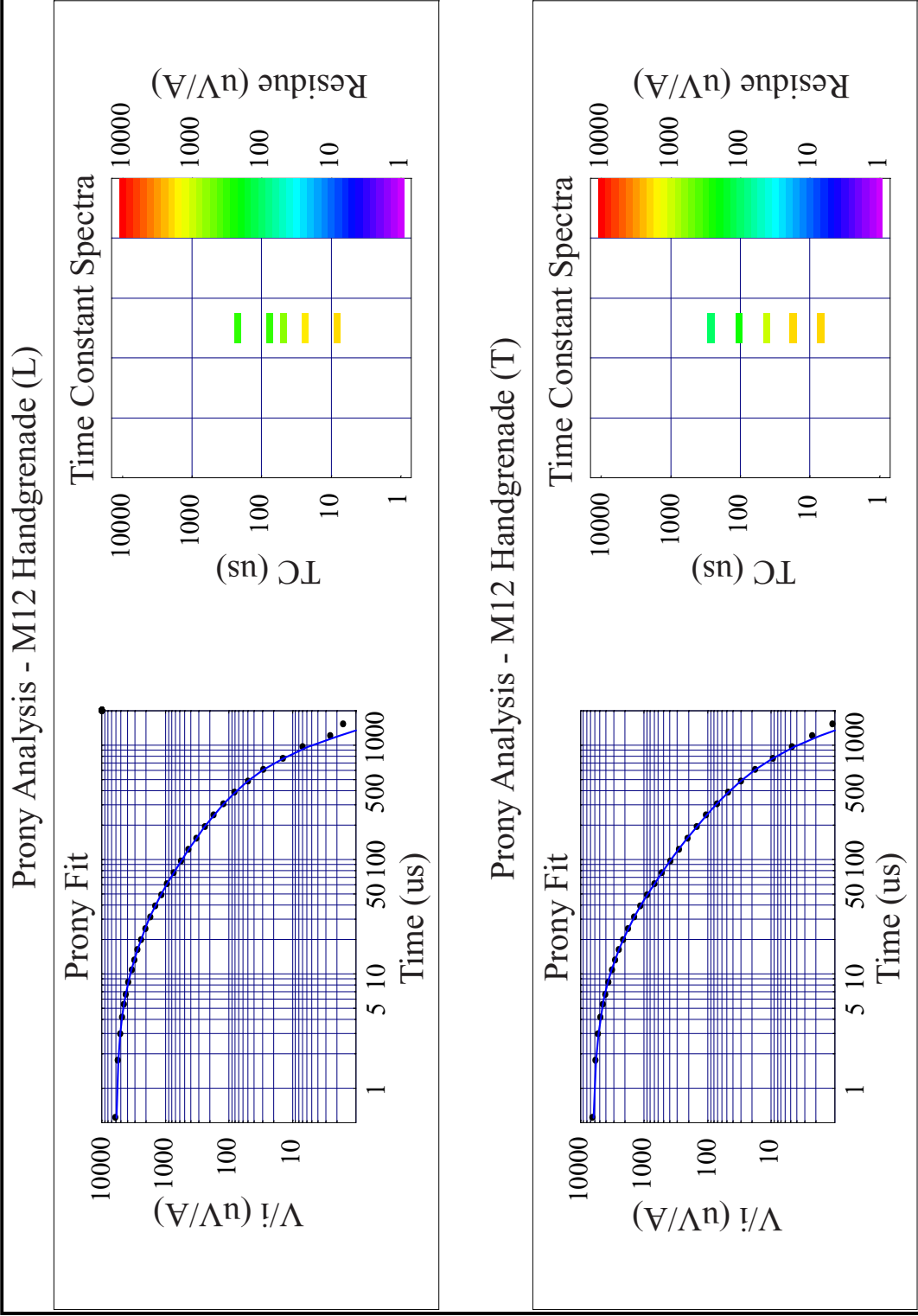
Figure 14: Prony analysis for TEM decay transients from an M12 handgrenade. The plot above is for longitudinal (L) polarization. The plot below is for transverse (T) polarization.
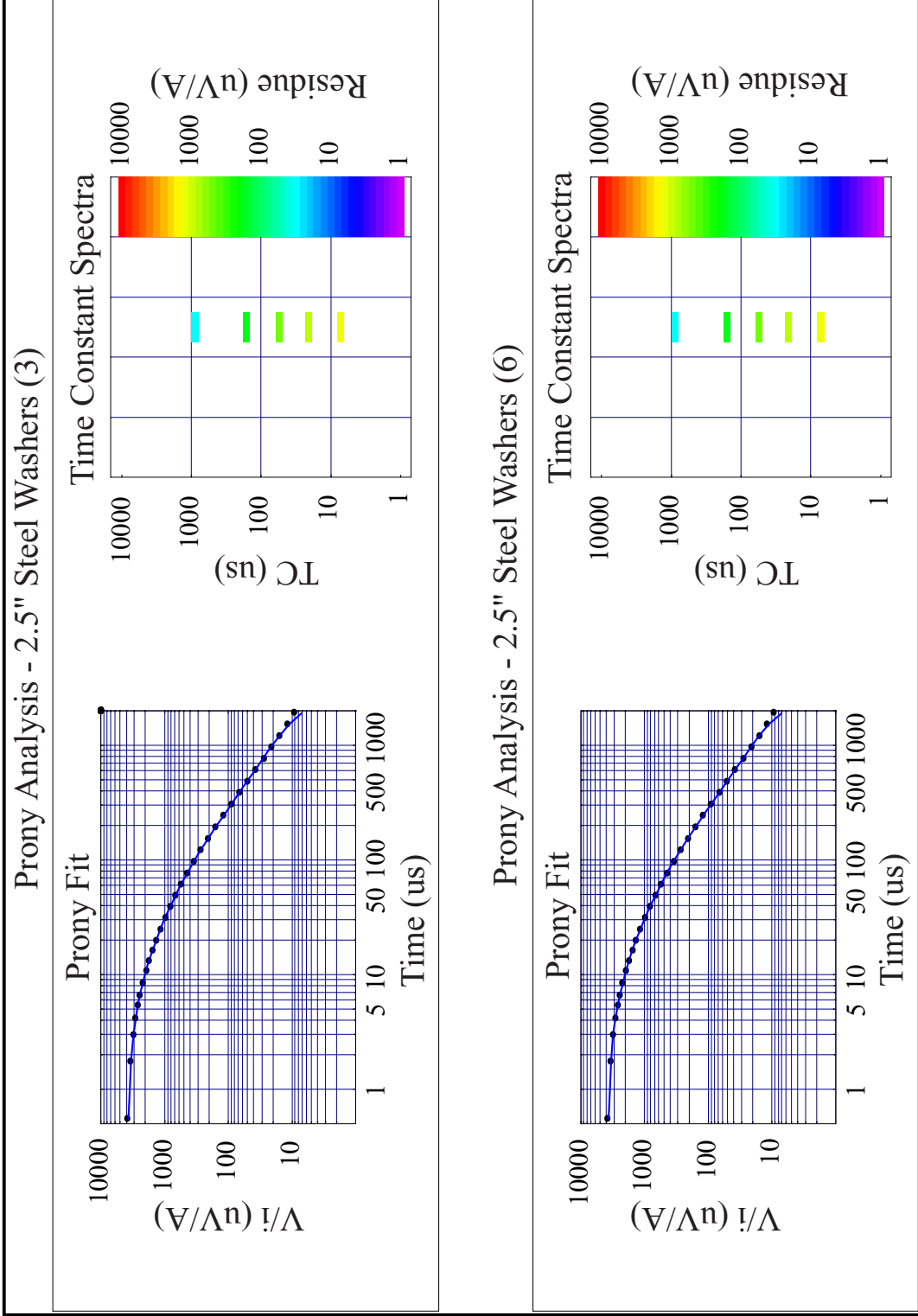
Figure 15: Prony analysis of TEM decay transients for stacks of 2.5" diameter steel washers. The plot above is for 3 washers. The plot below is for 6 washers.
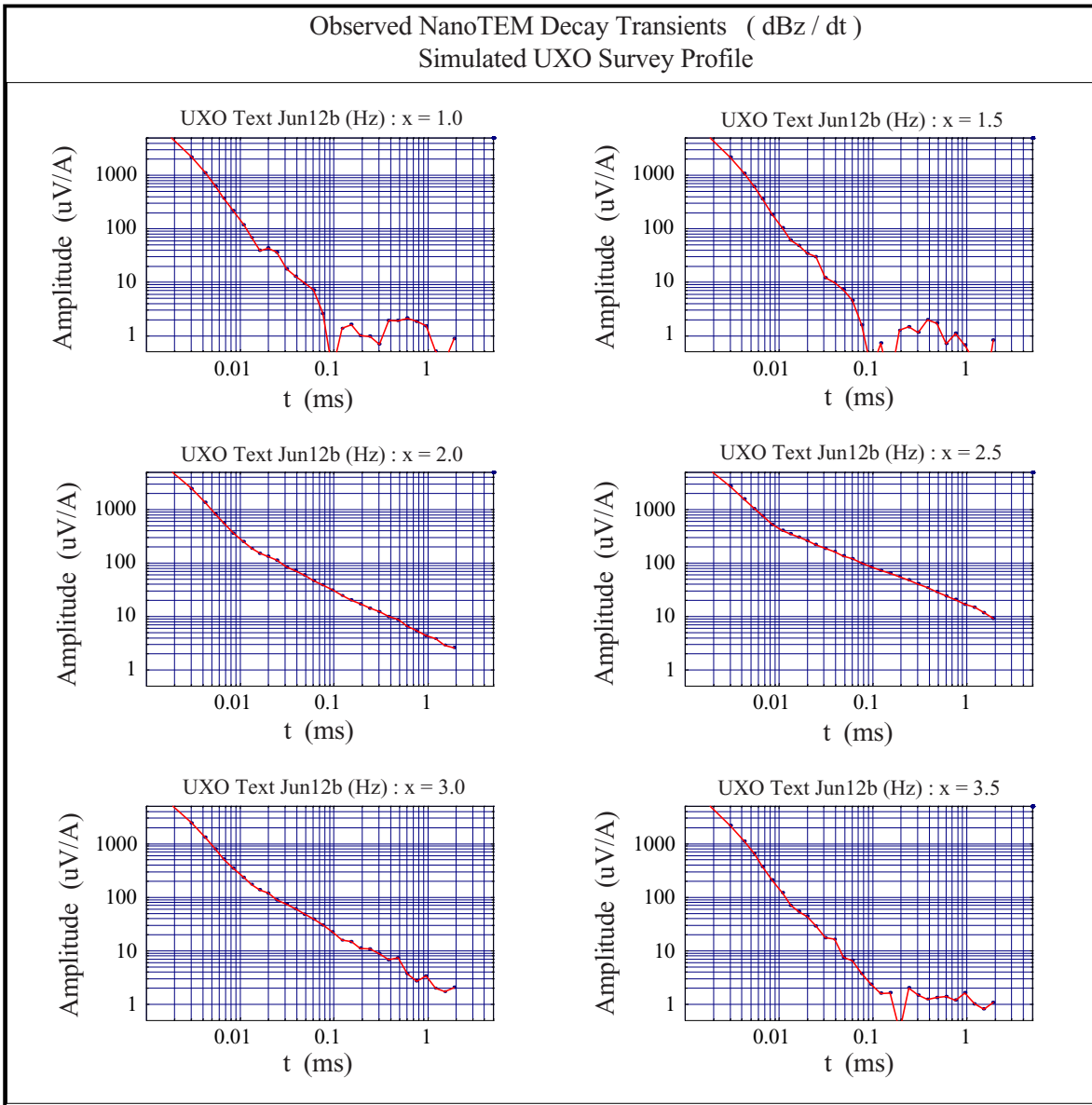
Figure 16: Observed NanoTEM decay transients. The transients were acquired at 1/2 m station intervals (x) along a profile over a UXO target buried at x=2.5m.
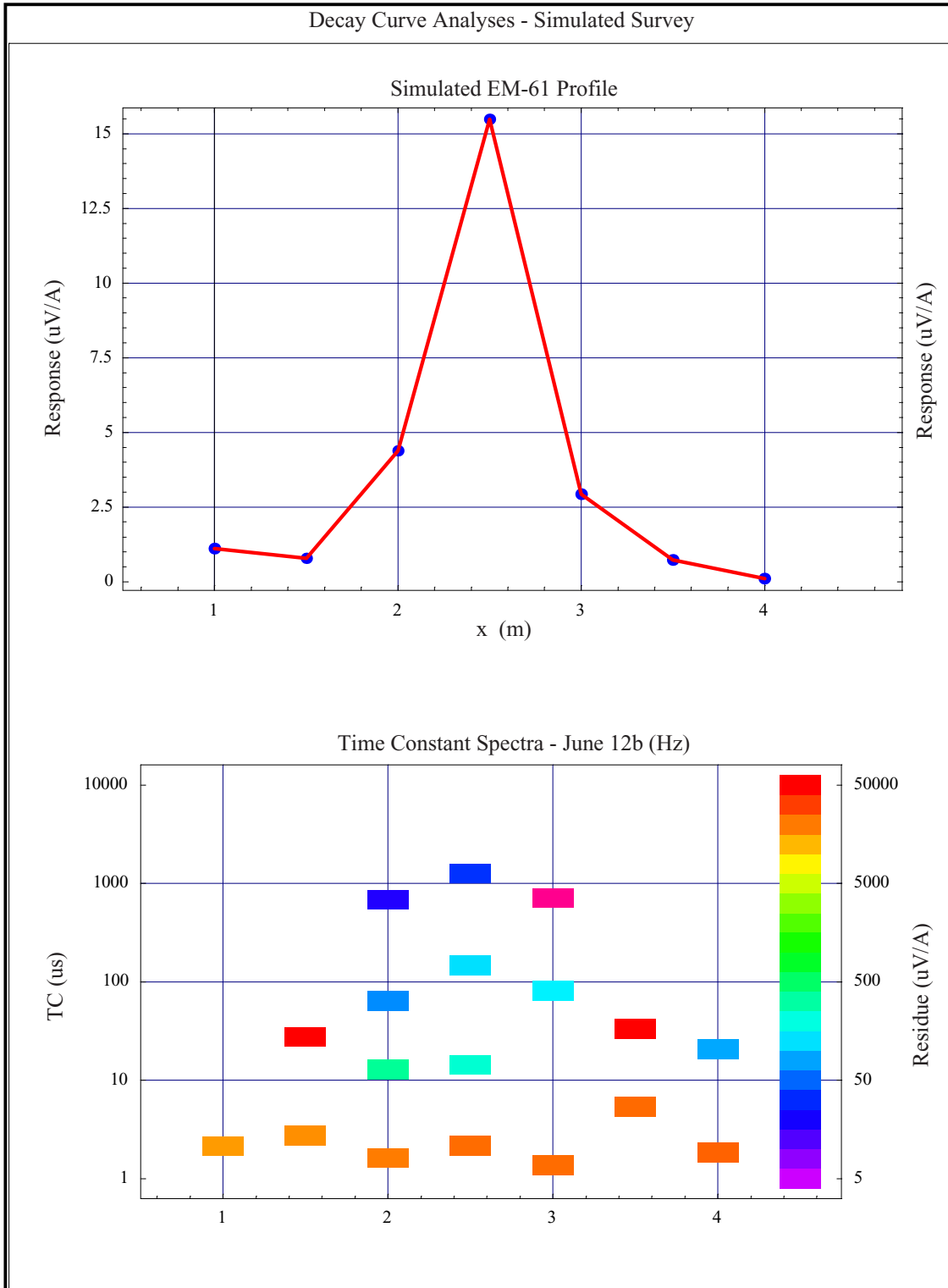
Figure 17: Results of a simulated UXO NanoTEM profile over a buried target. The curve above represents a synthetic EM61 response parameter computed by summing windows 24-31 of the decay curves. The bottom plot is the corresponding time constant spectra.